Journal of the European Ceramic Society xxx (xxxx) xxx

Contents lists available at ScienceDirect

Journal of the European Ceramic Society

journal homepage: www.elsevier.com/locate/jeurceramsoc

On the solubility of Bi in tetragonal tungsten bronzes

Caren Regine Zeiger, Benjamin Albert Dobson Williamson, Julian Walker, Mari-Ann Einarsrud, Tor Grande *

Department of Materials Science and Engineering, NTNU Norwegian University of Science and Technology, NO-7491 Trondheim, Norway

ARTICLE INFO

Keywords:
Lead-free
Tungsten bronzes
Dielectric properties
Ferroelectricity

ABSTRACT

Ferroelectric $Pb_5Nb_{10}O_{30}$ (PN) tetragonal tungsten bronze (TTB) forms solid solutions that exhibit morphotropic phase boundaries (MPBs). Successful replacement of PN with TTBs containing Bi could advance lead-free TTB MPBs. The most studied Bi containing TTB, $K_4Bi_2Nb_{10}O_{30}$, was recently demonstrated to be paraelectric, and we have systematically explored the possibility to increase the Bi-content beyond two Bi^{3+} ions per unit cell aiming to induce ferroelectricity. Higher Bi content was incorporated by either increasing the cation vacancy concentration on the A-site or by B-site substitution with lower valency cations. An additional pyrochlore phase was found in almost all the explored compositions exceeding two Bi^{3+} per unit cell. The instability of the TTB structure with higher Bi^{3+} concentrations was investigated in terms of first-principles calculations, combined with chemical considerations and including the tolerance factor. Consequently, an *in-plane* polarisation found in PN is unlikely to exist in Bi-based TTBs, meaning that Bi^{3+} cannot fully replace Pb^{2+} in ferroelectric TTBs.

1. Introduction

For the past 20 years, the European Commission has restricted the use of Pb [1], and since 2015 responsible consumption and production has been addressed by the United Nations sustainable development goals [2]. Although legally implemented, the actual replacement of the state-of-the-art Pb-based materials has not yet been achieved [3–5]. This is mainly due to the industry and consumers requiring at least equally well performing, if not out-performing materials, before a lead-free alternative is implemented. In the case of ferroelectric materials, the conventional material is $Pb(Zr_{1-x}Ti_x)O_3$ (PZT, $0 \leq x \leq 1$) [6–8], and the most common strategy for substitution of Pb focuses on mimicking the $6s^2$ lone pair effect of Pb, which is widely believed to be the source of superior polarization and piezoelectric properties of Pb-based material systems [9–11]. The most commonly used and realistic substitute for Pb^{2+} is Bi^{3+} [4,12–14], which is stable against oxidation, non-toxic and low cost, making it the primary choice of many lead-free compositions, such as $(Bi_{0.5}Na_{0.5})TiO_3$ [3,15], $Bi_4Ti_3O_{12}$ [15], $BiFeO_3$ [16], and $BiAlO_3$ [17].

The Bi-containing lead-free tetragonal tungsten bronzes (TTBs) $Ba_4Bi_2Ti_4Nb_6O_{30}$ [18], $Ba_2Bi_2Nb_{10}O_{30}$ [19–21], and $K_4Bi_2Nb_{10}O_{30}$ (KBN) [22] have recently been investigated. The crystal structure of TTBs offers a broad variety of cation sites, which creates opportunities for greater compositional engineering relative to perovskite ferroelectrics [23,24]. Possible ferroelectric properties of KBN have been suggested in previous works [25–29], and a first-principles study predicted an in-plane distortion (within the *a-b* plane) caused by the presence of lone pairs of Bi^{3+} [30]. However, our recent study has demonstrated that the crystal symmetry of both KBN and the related compound $Rb_4Bi_2Nb_{10}O_{30}$ (RBN) are centrosymmetric [22], demonstrating that neither of the two Bi-containing TTB compounds possess ferroelectric properties. It was hypothesized that ferroelectricity could be induced by increasing the total concentration of Bi^{3+} in the unit cell, since only two lone pair cations per unit cell are present in KBN, compared to five in ferroelectric $Pb_5Nb_{10}O_{30}$ (PN) [30]. As Bi is a group 15 element compared to Pb being in group 14, a different charge balance is required than for Pb-based compounds. Furthermore, Bi^{3+} is known to possess a less stereochemically active lone pair than Pb^{2+} [31].

Here, we report on the solubility of Bi in tetragonal tungsten bronzes. The work was motivated by the possibility of inducing ferroelectric properties in Bi-containing TTBs by increasing the Bi-content [22]. With KBN as a starting point, an increased Bi-content was explored by either increasing the cation vacancy concentration or substitution of Nb^{5+} with a lower valence cation (Ti^{4+}, Zr^{4+} or Fe^{3+}). A total of 13 different compositions were prepared, of which most attempts to increase the Bi-content beyond two Bi^{3+} per principle TTB unit cell resulted in the formation of a second phase with the pyrochlore crystal structure. Only two of the 13 compositions were single phase, corresponding to the

* Corresponding author.
E-mail address: tor.grande@ntnu.no (T. Grande).

https://doi.org/10.1016/j.jeurceramsoc.2024.01.005
Received 25 August 2023; Received in revised form 23 December 2023; Accepted 3 January 2024
Available online 6 January 2024

compositions $K_{3.5}Bi_{2.5}TiNb_9O_{30}$ (KB2.5TN) and $Ba_2Bi_2Nb_{10}O_{30}$ (BBN). It was demonstrated that the maximum possible Bi-content in TTBs is limited to slightly above two Bi^{3+} per unit cell. The low stability of the TTB phase with higher Bi-content is discussed with respect to the tolerance factor of the TTB structure [32,33] and supported by first principles calculations.

2. Materials and methods

2.1. Solid-state synthesis

Table 1 gives an overview of the nominal compositions of the synthesised materials, the abbreviation used for each composition along with the synthesis parameters. All the compositions were synthesised via the same two-step procedure [19], using the same raw materials from Sigma-Aldrich, where changes mainly occurred in the second step (precursor combination and sintering parameters). The conditions used for drying of the raw materials, ball-milling and calcination can be found elsewhere [19]. Heating rates for the precursor syntheses were 200 °C/h and 400 °C/h for sintering of the materials.

Using $K_4Bi_2Nb_{10}O_{30}$ as an example in the first step, the precursor synthesis comprised the reaction of stoichiometric amounts of K_2CO_3 (≥ 99.0 %, BioXtra) and Bi_2O_3 (99.9 %) with Nb_2O_5 (99.99 %) to give $KNbO_3$ and $BiNbO_4$. In the second step powder mixtures of the precursors $KNbO_3$, $BiNbO_4$, and Nb_2O_5 were mixed in a 4:2:2 molar ratio and sintered to give $K_4Bi_2Nb_{10}O_{30}$. The precursors $NaNbO_3$ and $RbNbO_3$ were synthesised using Na_2CO_3 (≥ 99.0 %, BioXtra) and Rb_2CO_3 (≥ 99.0 %, BioXtra) [19]. The precursor $Bi_4Ti_3O_{12}$ was prepared from Bi_2O_3 and TiO_2 (anatase, ≥ 99 %), where powders were mixed in a molar ratio of 2:3, while the $BiFeO_3$ and $BaNb_2O_6$ precursors were prepared from Bi_2O_3 and Fe_2O_3 (≥ 96 %), and from $BaCO_3$ (≥ 99 %) and Nb_2O_5, respectively, both in a 1:1 molar ratio. The powder mixes were dispersed in ethanol (isopropanol in case of $BiFeO_3$), ball-milled for 2 h and stripped of the respective solvent. The dried powder mixture was subsequently pressed into pellets, and $Bi_4Ti_3O_{12}$, $BiFeO_3$, and $BaNb_2O_6$ were calcined at 800 °C for 2 h [34], at 750 °C for 4 h [35], and at 1100 °C for 6 h [36], respectively. Additionally, ZrO_2 (99 %) was used as raw material in some syntheses.

2.2. Materials characterisation

Powders for X-ray diffraction (XRD) were prepared using a carbide mortar to grind the sintered pellets down to powders. Most XRD data were recorded at ambient conditions on a Bruker D8 A25 DaVinci instrument equipped with Cu Kα X-ray radiation (λ = 1.54 Å) using a divergence slit of 0.1°, a step size of 0.013°, and an acquisition time of 1 h. XRD patterns of KB2.33_N, BTN, and KBBN were recorded on a Bruker D8 Focus with a Cu Kα X-ray source and a LynxEye Super Speed detector using a divergence slit of 0.2°, 0.013 step size, and an acquisition time of 1 h. The diffractograms were analysed using software packages Diffrac.Eva 5.2 and Topas 6 from Bruker. Pawley refinements of the XRD data were carried out using Chebyshev polynomial expression for the background, sample displacement, and the fundamental parameter model for the peak shape. Pawley refinements with space group P4/mbm were used to determine the lattice parameters of single phase TTB compositions, while a $Fd\bar{3}m$ phase was added for samples containing an additional pyrochlore phase. Rietveld refinements were used to estimate the relative phase ratio between TTB and pyrochlore. Structural models for the two phases with space groups P4/mbm and $Fd\bar{3}m$ were taken from Nylund and Zeiger *et al.* [22] for KBN and from Hector and Wiggin [37] for $Bi_2Ti_2O_7$. The pyrochlore phase was assumed to have composition $KBiNb_2O_7$ so that one Bi^{3+} was replaced by K^+ and Ti^{4+} by Nb^{5+}. The background function was a minimal Chebyshev polynomial, while the peak shapes were refined based on the fundamental parameter model. Site occupancy was refined for single phase compositions, while the thermal parameters were not refined.

Scanning electron microscopy coupled with energy dispersive X-ray spectroscopy (SEM-EDX) was performed to elucidate the elemental composition of the phases present. Pellets of KB2.67□N, KB2.5□N, and KBFN were prepared for analysis by polishing down to 0.25 μm grit size and thermal etching at 1050 °C. Smoothly polished surfaces were difficult to obtain for KB*x*□N materials as KB2.67□N was prone to cracking and KB2.5□N prone to grain pull out and appeared moisture sensitive. SEM was performed on a Hitachi S-3400 N equipped with an Everhart-Thornley secondary electron detector operated at 5–15 kV. For SEM-EDX a working distance of 10 mm and an acceleration voltage of 15 kV were set before using an Oxford Instruments X-max 80 mm^2 detector in point analysis mode. Spectra of five points were measured and averaged for each observed feature.

Pellets with a diameter of 10 mm and a thickness of 1–2 mm were prepared for dielectric spectroscopy. The surface layer of ~ 0.1 mm of the pellets was removed before a thin layer of Pt paste (70 %, Gwent group, UK) was applied to both sides. The paste was dried for 15 min at 120 °C prior to its final heat treatment at 900 °C for 1 min with a heating rate of 200 °C/h to give the electrodes. Excess Pt around the edges was

Table 1
Overview of the sample label, nominal composition, precursors, molar ratio of the precursors and the sintering conditions (temperature and duration) of the synthesised compounds.

Sample ID	Nominal composition	Precursors	Precursor ratio	Sint. Conditions	
				Temp. [°C]	Time [h]
Filled TTBs					
NBN [22]	$Na_4Bi_2Nb_{10}O_{30}$	$NaNbO_3$, $BiNbO_4$, Nb_2O_5	4:2:2	1150	1
NKBN [22]	$Na_3KBi_2Nb_{10}O_{30}$	$NaNbO_3$, $KNbO_3$, $BiNbO_4$, Nb_2O_5	1:3:2:2	1150	1
KBN [22]	$K_4Bi_2Nb_{10}O_{30}$	$KNbO_3$, $BiNbO_4$, Nb_2O_5	4:2:2	1150	1
KBFN	$K_3Bi_3FeNb_9O_{30}$	$KNbO_3$, $BiNbO_4$, $BiFeO_3$, Nb_2O_5	3:2:1:2	1150	1
KB2.5TN	$K_{3.5}Bi_{2.5}TiNb_9O_{30}$	$KNbO_3$, $BiNbO_4$, TiO_2, Nb_2O_5	3.5:2.5:1:1.5	1150	1
KB3TN	$K_3Bi_3Ti_2Nb_8O_{30}$	$KNbO_3$, $BiNbO_4$, TiO_2, Nb_2O_5	3:3:2:1	1150	1
KBZN	$K_3Bi_3Zr_2Nb_8O_{30}$	$KNbO_3$, $BiNbO_4$, ZrO_2, Nb_2O_5	3:3:2:1	1150	1
RBN [22]	$Rb_4Bi_2Nb_{10}O_{30}$	$RbNbO_3$, $BiNbO_4$, Nb_2O_5	4:2:2	1150	8
RBTN	$Rb_{3.5}Bi_{2.5}TiNb_9O_{30}$	$RbNbO_3$, $BiNbO_4$, TiO_2, Nb_2O_5	3.5:2.5:1:1.5	1150	8
RBZN	$Rb_3Bi_3Zr_2Nb_8O_{30}$	$RbNbO_3$, $BiNbO_4$, ZrO_2, Nb_2O_5	3:3:2:1	1150	8
BTN	$Bi_6Ti_8Nb_2O_{30}$	$Bi_4Ti_3O_{12}$, TiO_2, Nb_2O_5	1.5:3.5:1	1150	1
Unfilled TTBs					
KB2.33□N	$K_3Bi_{2.33}Nb_{10}O_{30}$	$KNbO_3$, $BiNbO_4$, Nb_2O_5	3:2.33:2	1150	1
KB2.5□N	$K_{2.5}Bi_{2.5}Nb_{10}O_{30}$	$KNbO_3$, $BiNbO_4$, Nb_2O_5	2.5:2.5:2	1150	1
KB2.67□N	$K_2Bi_{2.67}Nb_{10}O_{30}$	$KNbO_3$, $BiNbO_4$, Nb_2O_5	2:2.67:2	1150	1
KB3□N	$K_1Bi_3Nb_{10}O_{30}$	$KNbO_3$, $BiNbO_4$, Nb_2O_5	1:3:2	1150	1
KBBN	$K_{0.5}BaBi_{2.5}Nb_{10}O_{30}$	$KNbO_3$, $BaNb_2O_6$, $BiNbO_4$, Nb_2O_5	0.5:1:2.5:2	1210	2
BBN	$Ba_2Bi_2Nb_{10}O_{30}$	$BaNb_2O_6$, $BiNbO_4$, Nb_2O_5	2:2:2	1240	2

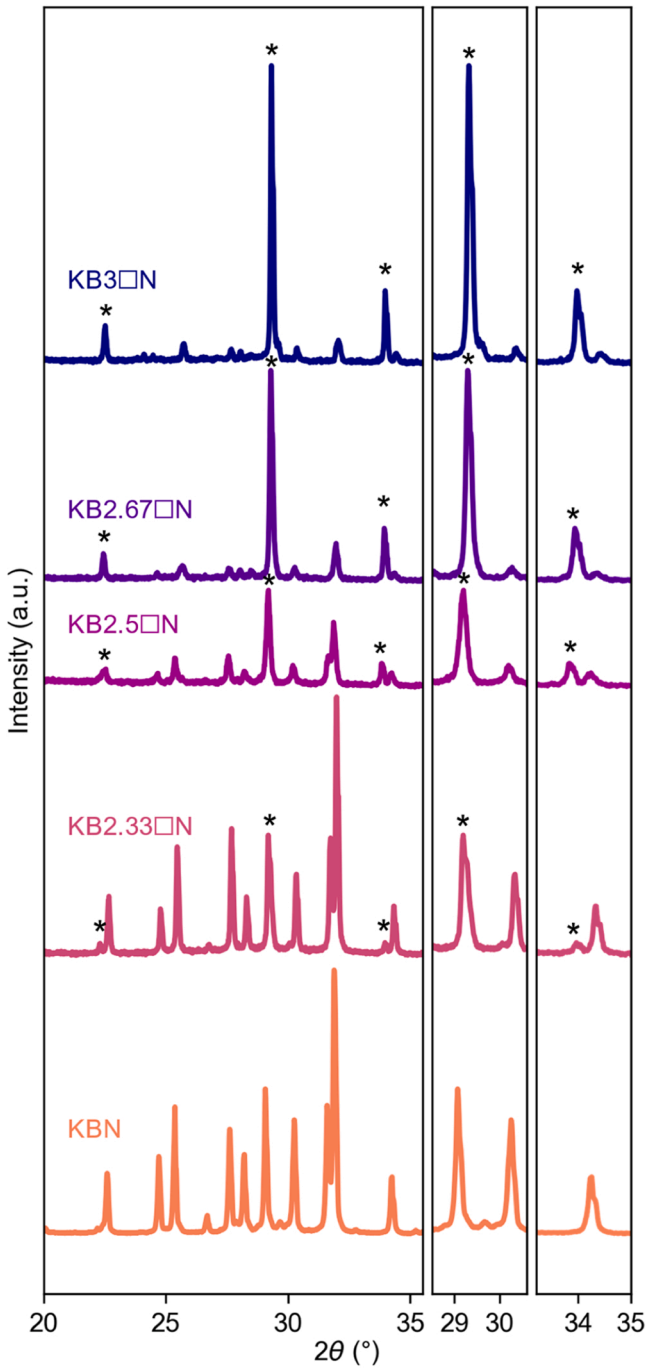

Fig. 1. XRD patterns of the KB*x*□N series including KBN [22], where asterisks mark additional reflections compared to the KBN pattern. The intensity of the patterns for KBN and KB2.33□N are scaled by a factor of 0.05 and 0.5, respectively. The full 2θ range of the patterns can be found in S3.

ground off prior to the experiments. A setup of an Alpha-A impedance analyser connected via two channels to a Novotherm testing chamber by Novocontrol was used to perform dielectric spectroscopy up to 400 °C, while a NORECS ProboStat sample cell situated inside a tubular furnace with a Eurotherm temperature controller with four-wire connection could measure up to 700 °C. Measurements were conducted using WinDETA software by Novocontrol with a heating rate of 2 °C/min and an AC voltage of 1 V.

Polarization-electric field measurements on pellets of 5 mm diameter and less than 0.5 mm thick with sputtered gold contacts were conducted at ambient temperature deploying the system aixPES by aixACCT.

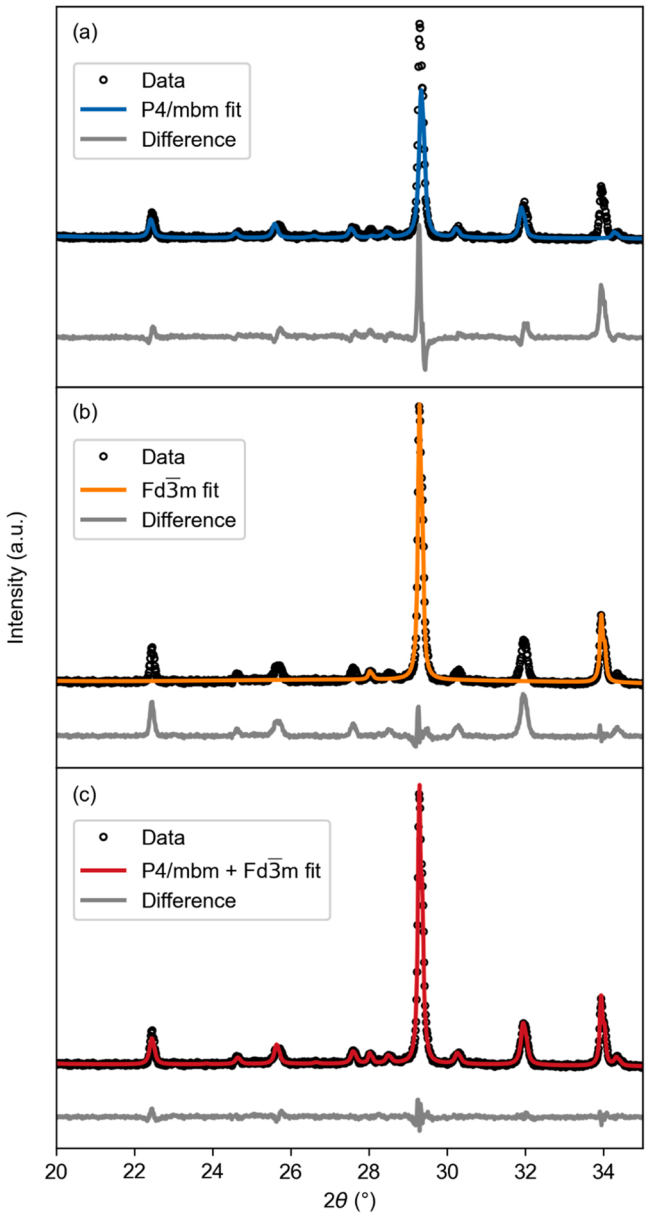

Fig. 2. Excerpt of the Pawley refinement of the diffraction data of KB2.67□N with (a) P4/mbm, (b) Fd$\bar{3}$m, and (c) P4/mbm and Fd$\bar{3}$m. The Pawley fit of the entire 2θ range can be found in S3.

Samples were submerged in silicone oil and contacted under slight tension while applying voltage pulses (100 Hz) with increasing field strengths until sample breakdown (max. up to 78 kV/cm).

2.3. Computations

All density functional theory (DFT) calculations were performed using the plane-wave code VASP (Vienna ab initio Simulation Package) [38–41]. The projector-augmented wave method (PAW) [42] was used to describe the interactions between the core and valence electrons for each Bi-based TTB composition which include Na [He], K [Ne], Rb [Ar], Bi [Xe], Nb [Kr] and O [He]. The Perdew-Burke-Ernzerhof gradient corrected functional revised for solids (PBEsol) [43,44] was used [43, 44], which has been shown to accurately describe the structural properties of tungsten bronzes [30,45–48], as well as thermodynamic stabilities of materials in general [49,50] relative to experiment. [49,50].

Initially, structural optimisation of the lattice parameters, and ionic

Table 2
Overview of the phases observed, phase content and lattice parameters of TTB (P4/mbm) and pyrochlore (Fd$\bar{3}$m) phases in all the samples studied.

Sample ID	Phases	Phase content /% TTB	Lattice parameters/Å		
			a_{TTB} /Å	c_{TTB} /Å	a_{pyro}/ $a_{perovskite}$ /Å
Filled TTBs					
NBN [22]	perovskite	0	-	-	3.92754(3)
NKBN [22]	TTB/perovskite	87	12.5126(3)	3.87985(11)	3.92754(3)
KBN [22]	TTB	100	12.6388(2)	3.92603(8)	-
KBFN	TTB/pyrochlore	62	12.6367(3)	3.92818(13)	10.5230(3)
KB2.5TN	TTB	100	12.6147(2)	3.91360(6)	-
KB3TN	TTB/pyrochlore	73	12.6062(3)	3.91283(10)	10.4875(3)
KBZN	TTB/pyrochlore	59	12.6628(5)	3.94037(18)	10.6451(3)
RBN [22]	TTB	100	12.7217(2)	3.95719(8)	-
RBTN	TTB/pyrochlore	39	12.7097(4)	3.95491(19)	10.5314(3)
RBZN	TTB/pyrochlore	0	-	-	10.5959(3)
BTN	TTB/pyrochlore	0	-	-	10.3830(1)
Unfilled TTBs					
KB2.33□N	TTB/pyrochlore	93	12.6138(2)	3.92631(9)	10.5592(8)
KB2.5□N	TTB/pyrochlore	70	12.6072(8)	3.93560(30)	10.5653(5)
KB2.67□N	TTB/pyrochlore	36	12.5290(9)	3.96308(41)	10.5643(3)
KB3□N	TTB/pyrochlore	30	12.4936(11)	3.95245(52)	10.5534(2)
KBBN	TTB/pyrochlore	91	12.5531(9)	3.93402(33)	10.5196(15)
BBN	TTB	100	12.5462(2)	3.92885(9)	-

positions of $R_4Bi_2Nb_{10}O_{30}$ (R = Na, K, Rb), in the P4/mbm spacegroup [22,30], were performed using a plane wave energy cut-off of 600 eV and a Γ-centred k-point grid of 2×2×6. Convergence was regarded as complete when the maximum force on any atom was below 0.01 eV $Å^{-1}$. Tabulated lattice parameters are provided in the supporting information S1. The addition of spin-orbit coupling showed minimal influence on the electronic structure and thus was not used in this study.

Determination of the thermodynamic stability of each Bi-containing TTB was carried out by calculating the "energy above the convex hull", requiring the relaxed structures of competing phases within the phase diagram. Starting structures were obtained from the materials project [51] and filtered based on both their stability/metastability (<0.09 eV [50,52]) and whether they are experimentally verified structures. Each competing phase was converged to the same force criterion as the parent compounds using a 600 eV plane wave energy cut-off and individually defined k-points. These are given alongside relaxed parameters for each individual competing phase in S1.

Additional calculations were carried out to understand the efficacy of the Bi lone pair within these materials. This involved density of states (DOS) calculations using both the PBEsol and the hybrid HSE06 functional shown in S2. HSE06 is known to more accurately represent the electronic structure compared to experiment, yet at an increased computational cost [53]. Isostructural Sb-containing TTB compositions were also calculated for comparison and are given in S2.

3. Results

3.1. Bi solubility and stability of the TTB phase

Diffraction patterns of the KBx□N ($x = 2.33, 2.5, 2.67, 3$) compositional series and KBN [22] ($x = 2$), are depicted in Fig. 1. A reduction of the intensity of the reflections corresponding to the TTB phase and the appearance of several new Bragg reflections are evident with increasing Bi-content. The effect is most prominent in the sample with the highest Bi-content (KB3□N). Pawley refinement of the XRD patterns using space group P4/mbm and the subsequent difference curves point to the formation of one or several new phases with increasing Bi-content in the KBx□N series. The new reflections, showing increased intensity with increasing Bi-content, were indexed successfully by a cubic pyrochlore phase with space group Fd$\bar{3}$m [37]. The X-ray diffraction patterns, beside the one for pure KBN, could therefore be indexed by a combination of TTB and pyrochlore phases as shown in Fig. 2 for KB2.67□N. Refinement of the diffraction patterns including two phases with the space groups P4/mbm and Fd$\bar{3}$m gave a good fit to the experimental data and can be found in S3. The space groups, phase content and lattice parameters determined by Rietveld refinement for the KBx□N compositions can be found in Table 2.

The relative phase content of the TTB and pyrochlore phases for the KBx□N series found by Rietveld refinement are displayed in Fig. 3a demonstrating a transition from the stable TTB phase to a pyrochlore phase through a two-phase region. Linear extrapolation of the relative phase content of the three compositions KB2.33□N, KB2.5□N and KB2.67□N suggests a Bi solubility limit at $x = 2.3$, indicated by the broken grey line.

The evolution of the unit cell parameters of the TTB and pyrochlore phases with increasing Bi-content in the KBx□N series is shown in Fig. 3b. The estimated Bi solubility limit at $x = 2.3$ from Fig. 3a separates the single phase TTB region from the two-phase TTB and pyrochlore region. A horizontal line was drawn for the lattice parameters in the single phase KBN region for simplicity due to lack of experimental observations in this phase region. A contraction of the a parameter and an expansion of the c parameter are observed with increasing nominal Bi-content. The lattice parameter evolution of the pyrochlore phase is also depicted, decreasing with increasing nominal Bi-content. Variation in the lattice parameters in the two-phase region demonstrates that the chemical composition of each of the two phases in equilibrium are not constant within this two-phase region.

Diffraction patterns of KBxTN ($x = 2.5, 3$) and BNT ($x = 6$) are presented in Fig. 4. KB2.5TN is single phase TTB, while KB3TN contains significant amounts of a similar pyrochlore phase as observed in the KBx□N series. A slightly higher Bi-content in the phase pure TTB composition could be obtained for KBxTN compared to KBx□N series. A two-phase region, consisting of coexisting TTB and pyrochlore phases, was also observed for this series at higher nominal Bi-content as summarised in Table 2. In BTN with nominally all six A-cation sites occupied by Bi^{3+}, no evidence of the presence of a TTB phase could be detected by XRD, illustrated by absence of the main reflection of space group P4/mbm at ~ 32°. Pawley refinement with a lower symmetry of the pyrochlore phase, i.e. space group P$\bar{4}$3m, could fit the whole pattern. Rietveld refinement with P$\bar{4}$3m gave a good fit to the pattern except some minor reflection marked with an asterisk. Based on the Rietveld refinement the composition of the pyrochlore was estimated to $Bi_{1.5}Ti_{1.5}Nb_{0.5}O_7$.

The diffraction patterns of the samples BBN, KBBN, KBZN, KBFN, RBTN and RBZN are shown with their Pawley refinements in S3. The identified phases, phase content and lattice parameters are summarised

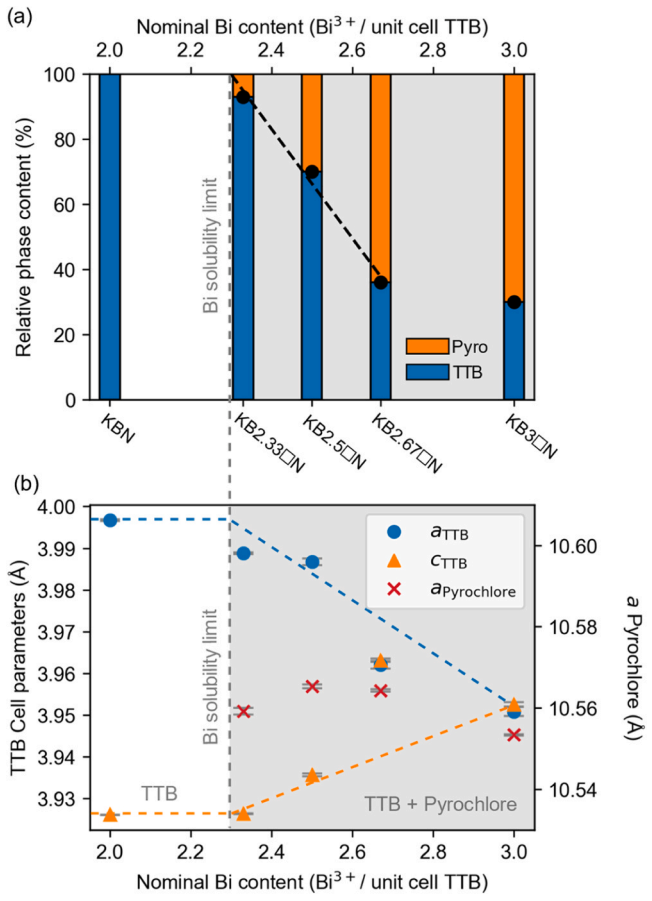

Fig. 3. (a) Relative phase content of TTB (blue) and pyrochlore (orange) estimated for the KB*x*□N series. The black dashed line is a linear regression of the phase contents to extrapolate the Bi solubility limit, which is illustrated by the grey broken line, and the mixed phase region of TTB and pyrochlore is shaded in grey. (b) Evolution of the unit cell parameters of the two phases as a function of the nominal Bi-content of the respective composition, where the coloured broken lines are guides to the eye. The a_{TTB} parameter was divided by $\sqrt{10}$. The uncertainty in the lattice parameters was found by Rietveld refinement.

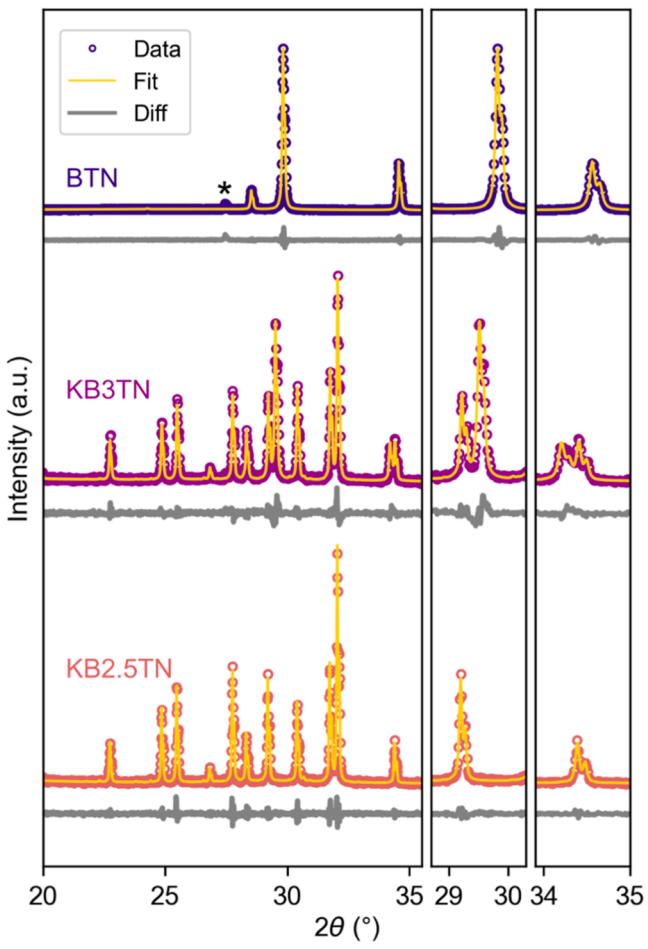

Fig. 4. Diffraction patterns of the KBxTN materials and BTN. Pawley refinement of KB2.5TN was performed with P4/mbm, while KB3TN was refined with both $Fd\bar{3}m$ and P4/mbm (yellow lines). The asterisk marks an additional reflection compared to the $P\bar{4}3m$ (yellow line) Rietveld refined phase found in BTN.

in Table 2. Again, TTB and pyrochlore phase were found coexisting for KBBN, KBZN, KBFN and RBTN. In case of RBTN additional reflections at low angles were observed, indicating that the symmetry or the unit cell size of the TTB phase changed. RBZN is similar to BTN almost single phase pyrochlore, while BBN was observed to be single phase TTB.

The estimated phase contents obtained via Rietveld refinement for all prepared samples are visualised in Fig. 5 together with the calculated tetragonality. The tetragonality is changing with the overall composition and the type of cations present, demonstrating that the chemical composition of the TTB phase does vary with the overall composition of the samples. This is also apparent in the SEM micrographs of KB2.67□N, KB2.5□N, and KBFN shown in Fig. 6. Two distinct different grain shapes and sizes were observed in both samples demonstrating the presence of co-existing TTB and pyrochlore phases. The morphology of KBFN is fundamentally different than that of the KB*x*□N materials. SEM-EDX was performed on these areas and the composition found by EDX is summarized in Table 3. SEM-EDX analysis of the two phases supports the varying chemical composition of the two co-existing phases with the overall composition of the samples.

In order to determine the thermodynamic stability of Bi-containing TTBs, DFT calculations were carried out on $Na_4Bi_2Nb_{10}O_{30}$, $K_4Bi_2Nb_{10}O_{30}$, and $Rb_4Bi_2Nb_{10}O_{30}$. All competing stoichiometric phases relating to their formation were relaxed and the energies used to contribute to an "energy above the convex hull". Each Bi-TTB

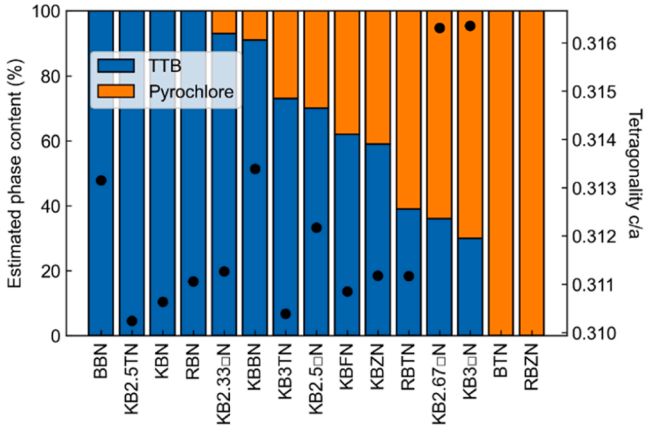

Fig. 5. Overview of the estimated TTB vs. pyrochlore phase content determined for all studied compositions (Table 2). Black markers denote the tetragonality (c_{TTB}/a_{TTB}) calculated from the lattice parameters of the TTB phase. Bars are sorted by decreasing TTB phase content.

composition was found to be metastable at 3×10^{-3} eV, 6×10^{-3} eV, and 1×10^{-3} eV above the convex hull, respectively (see S1). Therefore, no tangible trend was observed going to larger alkali cations on the

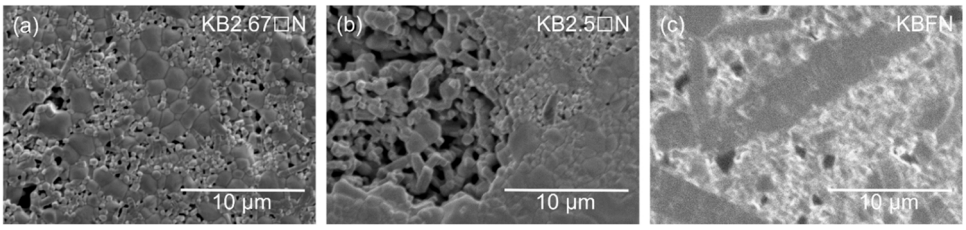

Fig. 6. SEM micrographs of (a) KB2.67□N, (b) KB2.5□N, and (c) KBFN.

Table 3
Elemental composition of grains in KB2.67□N, KB2.5□N, and KBFN determined by EDX and including the nominal composition. The grains observed by SEM is assigned to one of the two phases observed by XRD, which are TTB (T) or pyrochlore (P), respectively.

Sample		Bi at %	K at %	Fe at %	Nb at %	O at %
KB2.67_N	nominal	6.0	4.5	-	22.4	67.2
	large grains (T)	8.9(± 0.4)	4.1(± 0.4)	-	22.3(± 0.7)	64.7(± 2.9)
	small grains (P)	4.4(± 0.3)	5.2(± 0.4)	-	23.9(± 0.6)	66.5(± 2.7)
KB2.5_N	nominal	5.6	5.6	-	22.2	66.7
	large grains (P)	8.2(± 0.3)	3.8(± 0.5)	-	20.6(± 0.6)	67.3(± 3.1)
	small grains (T)	5.2(± 0.3)	5.8(± 0.5)	-	23.2(± 0.6)	65.8(± 3.0)
KBFN	nominal	6.5	6.5	2.2	19.6	63.5
	large grains (P)	5.5(± 0.4)	8.3(± 0.6)	0.6(± 0.5)	22.1(± 1.1)	63.5(± 5.1)
	small grains (T)	7.4(± 0.3)	6.9(± 0.5)	2.2(± 0.5)	20.2(± 0.6)	63.3(± 3.9)

thermodynamic stability. $Na_4Bi_2Nb_{10}O_{30}$ was found to be unstable towards $NaNbO_3$, Nb_2O_5, and $Na_3Nb_6Bi_5O_{24}$, while $K_4Bi_2Nb_{10}O_{30}$ and $Rb_2Bi_2Nb_{10}O_{30}$ were found to be unstable towards $NbBiO_4$, Nb_2O_5 and $RNbO_3$. Whilst this analysis predicts a slight metastability, it is important to note that both the parent and limiting phases are fully stoichiometric and ordered, which is not the case for pyrochlore phases, making them complex to calculate. However, these results highlight the fact that these compositions are on the edge of stability and thus it is likely that through disorder and non-stoichiometry these compositions will be stabilised, hence pyrochlore phases would be a possibility.

Fig. 7a–c shows the density of states (DOS) for $Na_4Bi_2Nb_{10}O_{30}$, $K_4Bi_2Nb_{10}O_{30}$, and $Rb_4Bi_2Nb_{10}O_{30}$, respectively. The upper valence band from ∼ −6 eV to 0 eV (valence band maximum, VBM) is predominantly made up of O 2p states with Nb 4d states showing the somewhat covalently bonded nature of the NbO_6 octahedral framework of the tungsten bronze structure. The VBM is dominated by localised O 2p states typical of wide band gap oxides such as TiO_2 [54]. The conduction band minimum (CBM) at ∼ 2.2 eV is on the other hand formed primarily of Nb 4d mixed with O 2p and 2s states. Isostructural

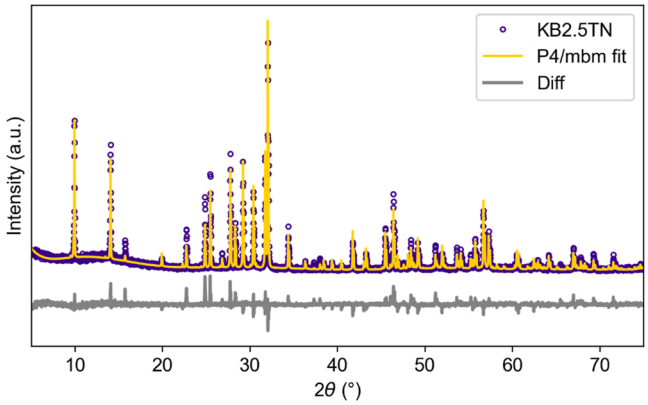

Fig. 8. Diffraction pattern of single phase TTB KB2.5TN together with the Rietveld refined fit using space group P4/mbm and difference between data and fit.

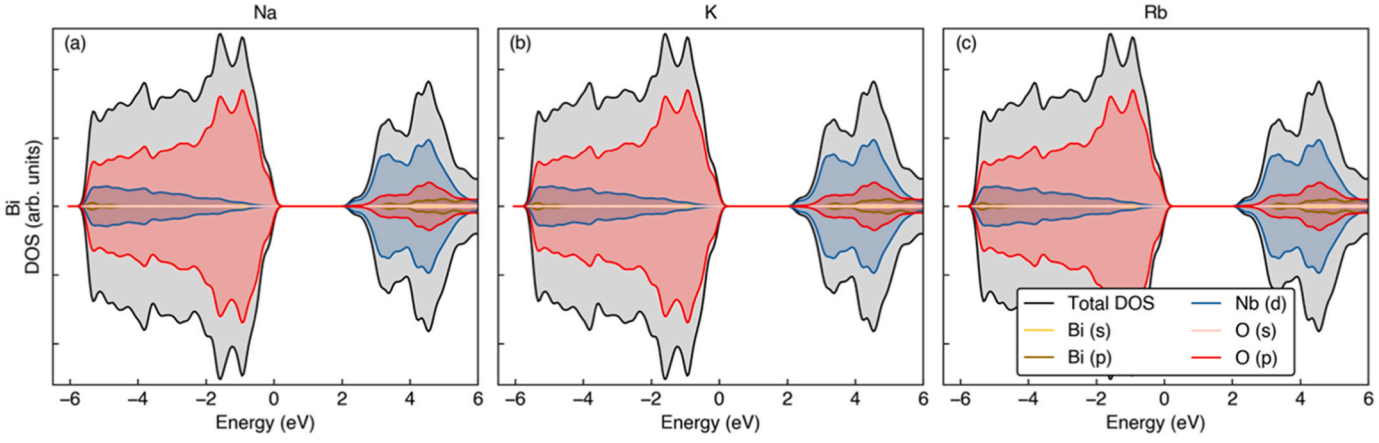

Fig. 7. The density of states (DOS) for $R_4Bi_2Nb_{10}O_{30}$ (R = Na, K, Rb) (a-c) calculated using the PBEsol functional. The valence band maxima (VBM) in each panel are set to 0 eV. In a material with a stereochemically active lone pair, the VBM would involve a covalency of O 2p + Bi6s and Bi 6p, however in this class of materials this is not the case.

Sb-containing TTBs were calculated to answer the question of whether a stereochemically active lone pair is possible within these compositions using a stronger lone-pair donor [31]. The results shown in S2 indeed demonstrate that the antibonding Sb s+p states are closer to the VBM and slightly more pronounced.

Fig. 8 shows the Rietveld refinements of the single phase TTB composition KB2.5TN, which has to our knowledge not been synthesised before. Rietveld refinement was performed with TTB aristotype space group P4/mbm, and all the reflections can be indexed using this space group for the TTB phase. The discrepancy of the intensities between the data and fit are most likely related to occupation of the different cation sites diverging from the nominal composition [22,36,45] and were minimized via refinement of the occupancy. Refinement details can be found in S4. The Rietveld refinement of BBN is in very good agreement with a previous report by Ma et al. [19], while Muktha et al. [21] did not obtain single phase material with a slightly higher sintering temperature (1240 °C vs. 1250 °C).

3.2. Electrical properties of single-phase samples

Dielectric permittivity and loss as a function of temperature are shown in Fig. 9 for single phase TTB KB2.5TN. For frequencies of 10^4 Hz and above, a broad and slightly frequency dispersed maximum in dielectric permittivity is apparent with its peak at approx. 250 °C. The shape is similar to recently collected data of KBN [22]. Increasing dielectric losses are observed both with increasing temperature and decreasing frequencies, indicating the onset of conduction at elevated temperatures. Around ambient temperature a second loss peak can be observed for frequencies above 10^5 Hz, shifting to lower temperatures with decreasing frequency, possibly pointing to an additional low-temperature local maximum in dielectric permittivity.

Polarisation-Electric field loop at ambient conditions for KB2.5TN is presented in Fig. 10 alongside data on KBN [22] (inset). The loop taken at 70 kV/cm, just below breakdown field (76 kV/cm), exhibits a slight non-linearity compared to the linear dielectric response of KBN. The degree to which the response is linear is emphasised by comparison with the broken grey line drawn through the centre of the loop. While the small degree of nonlinearity is itself not sufficient to indicate ferroic properties, it is perhaps reminiscent of the beginnings of a relaxor-type behaviour, where the P-E loop remains narrow with little remanent polarization but becomes more nonlinear as it approaches saturation at high electric fields. If a relaxor-like behaviour was more prominent, its

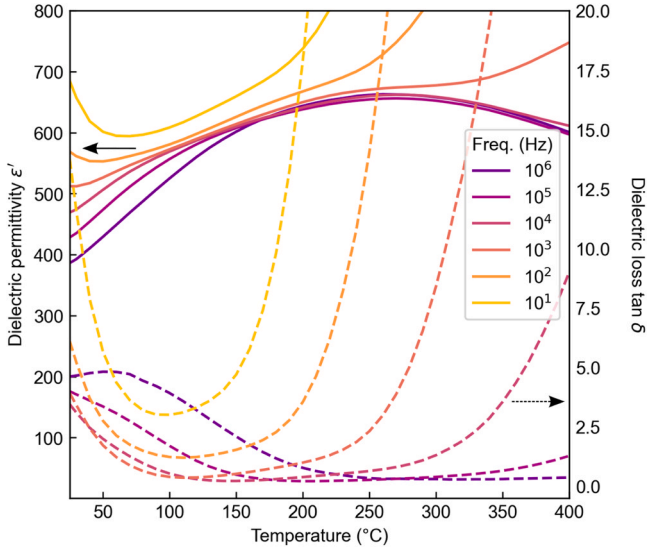

Fig. 9. Temperature dependent evolution of dielectric permittivity (full lines) and electrical loss (broken lines) for KB2.5TN.

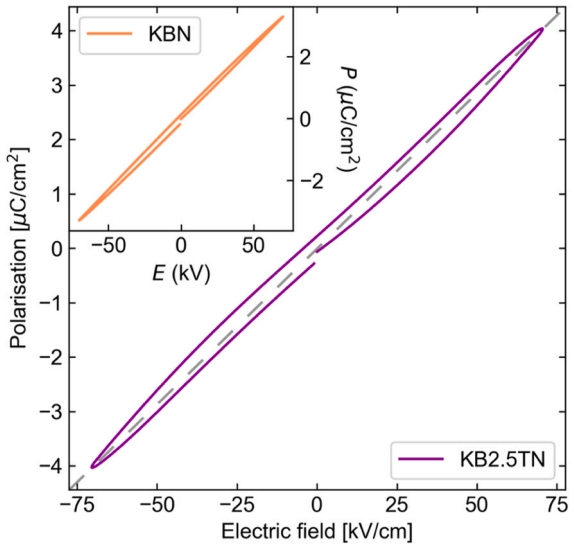

Fig. 10. Polarisation-Electric field loop of KB2.5TN recorded at ambient temperature with 70 kV/cm and 100 Hz. The broken grey line was added to emphasise the slightly non-linear behaviour of KB2.5TN. Data for KBN [22] shown in the inset for comparison.

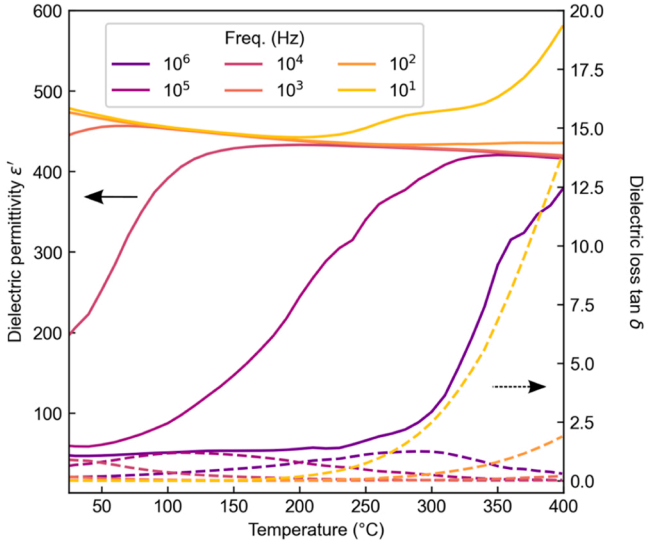

Fig. 11. Dielectric data of BBN displaying the dielectric permittivity in full lines and the electrical loss in broken lines.

appearance could be connected to the weak frequency dispersion observed in dielectric permittivity (Fig. 9) [55]. Hence, a minor increase of Bi appears to cause a measurable difference of polarisation response when subjected to an electric field in case of KB2.5TN, and perhaps the true nature of the behaviour would become evident if the material could withstand higher electric fields. Additional P-E loops collected of KB2.5TN are shown in S5.

Dielectric permittivity and loss as a function of temperature for BBN is depicted in Fig. 11. The permittivity behaviour differs significantly from that of KB2.5TN, showing a step-plateau feature instead of a local maximum as a function of temperature. Though similarly, BBN displays a significant frequency dispersion reaching from ambient temperatures up to 400 °C for the frequency range 10^3–10^6 Hz. The step-like increase in permittivity is indicative of introduction of additional mechanisms contributing to the response with increasing temperature. One possibility are additional dipole moments from defect couples, also explaining the frequency dispersion of the response [56,57]. Increase in the

electrical loss is accompanied by steep increases in dielectric permittivity indicating the onset of conduction at elevated temperatures (see S5 for temperatures up to 600 °C). Dielectric spectroscopy has been performed on BBN before [19,20] and the reported shape aligns well with this work. However, the significant frequency dispersion was not reported for BBN before and differs from the one measured by Simon and Ravez [20], the most apparent difference to their material being a 140 °C higher sintering temperature (1100 °C vs. 1240 °C).

Polarisation-Electric field loops for BBN are shown in S5, demonstrating purely dielectric behaviour up to its breakdown field strength at 95 kV/cm and 250 °C.

4. Discussion

In our previous work it was hypothesised that the Bi-content in KBN was too low to display ferroelectric behaviour, and if the Bi-content could be increased, in-plane polarisation similar to PN could possibly be induced [22]. In this work, we have demonstrated that the Bi^{3+} solubility in TTBs is strongly limited, and realisation of ferroelectric Bi-rich TTBs is not likely. We recently demonstrated that the crystal structure of KBN is centrosymmetric [22], contradicting preceding studies reporting on its ferroelectric nature [25,27,30,33]. Based on structural analogy with PN, KBN was referred to as possessing the same functional properties, i.e., ferroelectricity [25]. PN contains five Pb^{2+} per unit cell and is an unfilled TTB, while KBN contains two Bi^{3+} and four K^{+}, making it a filled TTB. This makes them chemically quite distinct, specifically considering that Bi^{3+} possesses a stereochemically less active lone-pair than Pb^{2+} [31], and Pb^{2+} off-centring was identified responsible for the observed in-plane polarisation in PN [30]. Most TTBs feature an out-of-plane polarisation mechanism, such as $Sr_xBa_{5-x}Nb_{10}O_{30}$ (SBN) [47] and $Ba_4Na_2Nb_{10}O_{30}$ (BNN) [46]. Hence, a lead-free TTB with *in-plane* polarisation could take the engineering of lead-free TTB solid solutions exhibiting morphotropic phase boundaries (MPBs) to the next level.

The Bi solubility limit was determined for all the composition series studied in this work. The formation of an additional pyrochlore phase was apparent from the XRD patterns, and the pyrochlore phase content was increasing with increasing nominal Bi-content (Table 2 and Fig. 5). In the two-phase region in Fig. 3b, where the two phases coexist, their compositions change as evidenced by their changing lattice parameters. Similarly, SEM-EDX (Table 3) demonstrates that the chemical composition of the TTB phases found in KB2.5□N and KB2.67□N differ from each other as well as from the nominal composition. Thus, there is no stable TTB phase capable of incorporating more Bi^{3+} and instead an additional pyrochlore phase is formed. This can be explained by the increased chemical complexity of the solid solutions and thereby the possibility for more degrees of freedom according to Gibbs phase rule [58].

The TTB framework is closely related to the perovskite structure [24] and we analyse our observations in relation to the structural stability diagram of ABO_3 reported by Giaquinta and zur Loye [59] as shown in Fig. 12a. The stability of the TTB phase was analysed via the correlation of the A- and B-site ionicities $(\Delta\chi_{M-O})(r_M/r_O)$, where χ describes the electronegativity, r is the ionic radius and M indicates A- or B-site. In presence of several A- and B-site cations, average radii and electronegativities were used, cf. S6. The structural stability diagram outlined for TTBs in Fig. 12b shows a two-phase region separating the stability region of TTB and pyrochlore crystal structures. In the two-phase region, both phases coexist. In contrast, only stoichiometric ABO_3 compounds were considered by Giaquinta and zur Loye [59], where a two-phase region would not be possible according to the Gibbs phase rule [58]. Formulated in its reduced form (constant pressure), the Gibbs phase rule is defined as $F = C - Ph + 1$, where F defines the degrees of freedom, C is the number of components, and Ph is the number of phases present in the system. In case of ABO_3, with a fixed stoichiometry, $C = 1$, and consequently $F = 0$ when $Ph = 2$. Considering now the TTBs studied here, without a fixed composition, $F > 0$ when $Ph = 2$ and two or even more phases can be coexistent at a given overall composition. Instead of generating a sharp phase boundary between TTB and pyrochlore phase, a two-phase region results. This is also evidenced by the SEM-EDX analysis, showing a variable composition of both TTB and pyrochlore

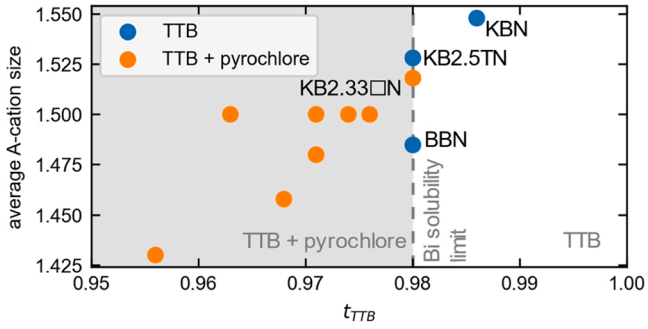

Fig. 13. Correlation between average A-cation size and the TTB tolerance factor [32,33] for the K-based TTBs including BBN. The broken grey line indicates the observed Bi solubility limit at $t_{TTB} = 0.98$ for K-based Bi TTBs and divides the area of the graph into single phase TTB and mixed TTB and pyrochlore phases. See S6 for information on the data points.

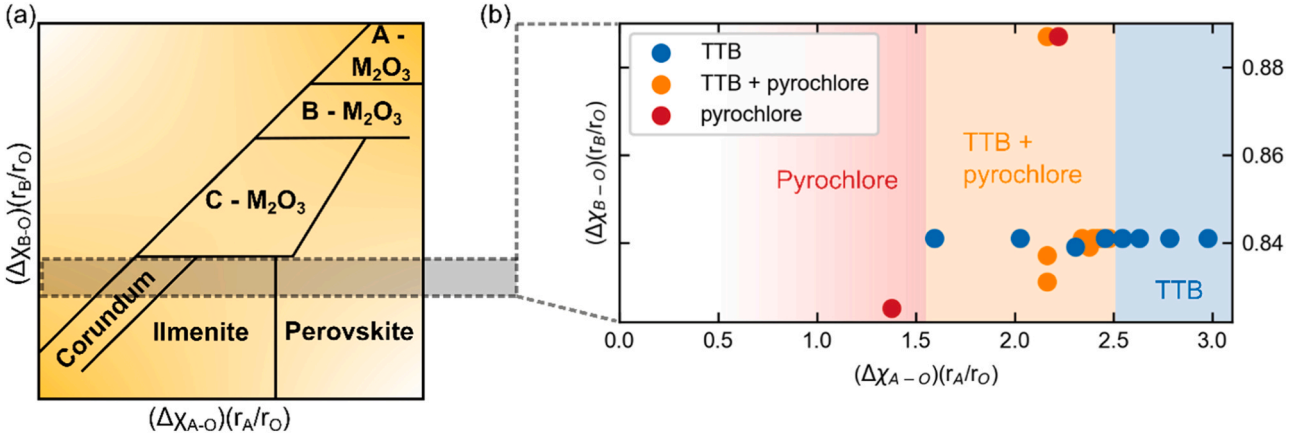

Fig. 12. (a) Structural stability diagram for ABO_3 compounds, adapted from Giaquinta and zur Loye [59], correlating A- and B-site cation ionicities $(\Delta\chi_{A-O})(\overline{r_A}/r_O)$ and $(\Delta\chi_{B-O})(\overline{r_B}/r_O)$, where χ describes the electronegativity. (b) Structural stability diagram constructed for the compositions synthesised in this work and some additional single phase TTBs [22,30,36,60]. See S6 for information on the data points.

phase (Fig. 6 and Table 3).

Further explanation for the instability of the TTB phase with increased Bi-content is found when mapping the average A-cation size against the tolerance factor t_{TTB} (for TTBs) [32,33] as shown in Fig. 13. For the K-based TTBs the figure illustrates that below $t_{TTB} = 0.98$, there are no stable single phase TTBs. Increasing the Bi-content lowers t_{TTB}, and consequently, at a certain limit, Bi becomes too small to facilitate the TTB structure. Bi^{3+} with an ionic radius of 1.36 Å (coordination number (CN) = 12) [61] is too small to be incorporated with high concentrations into TTBs as t_{TTB} is decreasing with increasing Bi-content. Similarly, NBN and NKBN [22], exhibiting pure perovskite and mixed perovskite and TTB phases with 4 and 3 cations Na^+ (1.39 Å, CN = 12) per unit cell TTB, respectively, were also not observed to form single phase TTBs. This points to a limit of average cation size required to facilitate the TTB phase and could possibly be deduced from the data published by Hardy *et al.* [62]. KB2.33□N lies at the Bi solubility limit (Fig. 13) and contains a pyrochlore phase in addition to the dominant TTB phase. In contrast to KB2.5TN which also has $t_{TTB} = 0.98$ but is phase pure, KB2.33□N features cation vacancies, though their size and effect on the TTB structure have not been studied in detail so far. BBN also lies on the Bi solubility limit, however, is single phase TTB and contains more cation vacancies than KB2.33□N, hence illustrating the influence of cation vacancies on the TTB structure. Gardner and Morrison [63] previously pointed out that cation vacancies may have a substantial effect on the functional properties of TTBs due to their size. The presented stability considerations on Bi-TTBs using the tolerance factor works well, despite the lack of understanding the effect of cation vacancies on A1- and A2-sites. Similar to what has been established for perovskites, where the size relation between A- and B-site cations and their effect on the tolerance factor has been studied in depth and is used to predict new compositions [64–67], the tolerance factor is a useful tool for TTBs as previously demonstrated by Zhu et al. for the functional properties of TTBs [33]. So far, the results point to a narrower stability window for TTBs compared to perovskites, at least in the region $t_{TTB} < 1$ of the stability range.

Several different alternatives to prepare Bi-rich TTBs were employed in this work, and they are summarised in Fig. 14. It shows the different chemical pathways to increase the Bi content, pointing out that KB2.5TN was the only single phase TTB with increased Bi-content. All the other compositions resulted in formation of an additional phase (Fig. 5). KB2.5TN was determined to exhibit a centrosymmetric structure (Fig. 8), though it displayed a slight relaxor-like behaviour in contrast to KBN, both by dielectric spectroscopy and polarisation-electric field measurements. The emerging non-linearity is most likely connected to the increased lone-pair concentration, though still too low to cause a polar structure, at least at macroscopic level [68]. Therefore, if ferroelectricity can be induced by an increased Bi^{3+} concentration, it would require more Bi^{3+} than incorporated in KB2.5TN, though not achievable due to the lack of stability of the TTB crystal structure.

Since the early 2000 s, when the implementation of Pb into electronic appliances was restricted, Bi-based materials have been one of the top choices to establishing lead-free ferroelectrics. Bi is positioned next to Pb in the periodic table, also possessing a $6s^2$ lone-pair with similar polarizability [69], though it is non-toxic despite being a heavy metal. Most engineering attempts focusing on Pb replacement by Bi, encompass material systems such as $Bi_{0.5}Na_{0.5}TiO_3$ [3,70], $BaTiO_3$-$BiMO_3$ (M = metal cations with an average +3 charge) [71,72], $BiFeO_3$ [16,73] or layered bismuth titanate structures [74], while KBN [22,25,27,30,33], BBN [19–21] and $Ba_4Bi_2Ti_4Nb_6O_{30}$ [18] are the lead-free TTBs containing Bi which have been investigated so far. The successful replacement of Pb with Bi in perovskites has motivated a corresponding replacement of Pb by Bi in TTBs [4]. Outlined by Walsh et al. [31], bonding between Bi 6s states and O 2p states gives rise to antibonding Bi s - O p states at the top of the valence band which are additionally stabilised by Bi 6p, thus giving rise to a stereochemically active lone pair causing non-centrosymmetry. From our calculations, it is shown that the Bi 6s and 6p states are minimal (< 1 %, Fig. 7). This is likely a result of several factors, such as having a small number of Bi^{3+} per unit cell, the domination of the valence band by Nb-O bonding, as well as the strength of the Bi lone pair [31]. Previous work confirms centrosymmetry, aiding these findings [22]. It is known that PN is non-centrosymmetric due to an in-plane polarisation arising from a stereochemically active lone pair [30], thus due to Bi's lower lying 6s and 6p states it is unlikely that a similar behaviour would be seen for Bi-TTBs. Bi has proven capable of causing distorted structures such as evidenced by the diverse lead-free Bi-based systems studied in literature [16,70,74,75]. The concentration of Bi per unit cell of the perovskite-based systems, however, is much higher than found in the KBN-related TTBs studied in this work and it proved impossible to substantially increase the Bi-content for TTBs due to a solubility limitation of Bi in the TTB framework. Sb-TTBs were briefly studied and expected to have a more preferential overlap between 5s +5p and O 2p states, and indeed the calculations show that the antibonding Sb 5s +5p states are closer to the VBM and slightly more pronounced (S2). However, the effect would still be very weak due to the

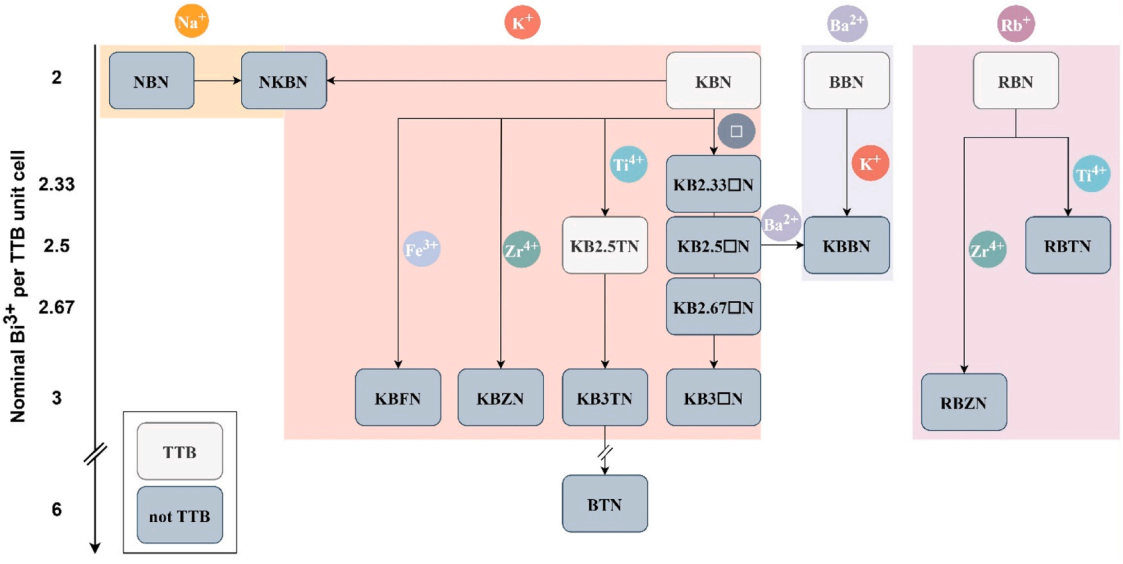

Fig. 14. Overview of materials synthesised in this work and their compositional relations. Added cations or vacancies (A- or B-site) are written on the connecting arrows. Coloured boxes indicate compositions based on the different alkaline (earth) metals Na^+, K^+, Rb^+ or Ba^{2+}.

low concentration of Sb in the system, further diluted due to the multivalency of Sb, and thus site distribution within the unit cell.

5. Conclusion

Several KBN related compositions with increased nominal Bi-content were prepared to investigate whether an increased Bi-content would induce ferroelectricity in Bi containing TTBs. All the different approaches to compositionally engineer an increased Bi-content in TTBs resulted in the appearance of an additional pyrochlore phase, demonstrating the low solubility limit of Bi^{3+} in the TTB structure. The lack of stability of TTBs with higher Bi-content was explained by a low tolerance factor and supported by first principles calculations. With increasing nominal Bi^{3+} concentration, the pyrochlore phase content increased accordingly on the expense of the TTB phase. A two-phase region with coexisting TTB and pyrochlore phases was determined, and these observations were analysed taking inspiration from the work by Giaquinta and zur Loye [59] on structural predictions of ABO_3 compounds. Finally, a new single-phase TTB, $K_{3.5}Bi_{2.5}TiNb_9O_{30}$, was synthesised and its crystal structure and dielectric properties were determined. It possesses a centrosymmetric space group, and its dielectric response was relaxor-like.

Declaration of Competing Interest

The authors declare that they have no known competing financial interests or personal relationships that could have appeared to influence the work reported in this paper.

Acknowledgment

Financial support is given by the Norwegian Research Council (project High-Temperature Lead-Free Ferroelectrics based on Tungsten Bronzes (301954)). Computational resources were also provided by UNINETT Sigma2 through Project NN9264K. The authors thank Nora Statle Løndal, Ola Gjønnes Grendal, and Sverre Magnus Selbach for inspiring scientific discussions.

Author Contributions

Caren Regine Zeiger (CRZ) performed all the experimental work, supervised by Tor Grande (TG), Mari-Ann Einarsrud and Julian Walker. CRZ wrote the first draft to the manuscript with contributions from TG and Benjamin Albert Dobson Williamson (BADW). BADW provided the shown DFT calculations. All authors contributed to the review and editing of the final manuscript and have given approval to the final version of the manuscript.

Appendix A. Supporting information

The supporting information includes the following information: Thermodynamic stability calculations, computations of the electronic structure, full 2θ-range XRD patterns with Pawley refinements complementing the data shown in the article, Rietveld refinement details, complementary electrical data including dielectric spectroscopy and P-E loops, data points for the stability diagram of the TTB phase, and data points for tolerance factor modelling. Supplementary data associated with this article can be found in the online version at doi:10.1016/j.jeurceramsoc.2024.01.005.

References

[1] Directive 2002/96/EC of the European Parliament and of the Council of 27 January 2003 on waste electrical and electronic equipment (WEEE) - Joint declaration of the European Parliament, the Council and the Comission relating to Article 9. OJEU - L, 2003, *37*, 24–39.

[2] United Nations, Resolution adopted by the General Assembly of the United Nations on 25th September 2015: Transforming our world: the 2030 Agenda for Sustainable Development, 2015, 77th General Assembly, 35.

[3] R.-A. Eichel, H. Kungl, Recent Developments and Future Perspectives of Lead-Free Ferroelectrics, Funct. Mater. Lett. 03 (2011) 1–4.

[4] J. Rödel, W. Jo, K.T.P. Seifert, E.-M. Anton, T. Granzow, D. Damjanovic, Perspective on the Development of Lead-free Piezoceramics, J. Am. Ceram. Soc. 92 (2009) 1153–1177.

[5] D. Damjanovic, N. Klein, J.I.N. Li, V. Porokhonskyy, What can be expected from lead-free piezoelectric materials? Funct. Mater. Lett. 03 (2011) 5–13.

[6] B. Jaffe, W.R. Cook, H. Jaffe, Piezoelectric Ceramics, Academic Press, London, 1971.

[7] N. Setter, Piezoelectric Materials in Devices: Extended Reviews on Current and Emerging Piezoelectric Materials, Technology and Applications, N. Setter, Lausanne, 2002.

[8] A.J. Moulson, J.M. Herbert. Electroceramics: Materials, Properties, Applications, 2nd ed., Wiley, Chinchester, 2003.

[9] R.E. Cohen, Origin of ferroelectricity in perovskite oxides, Nature 358 (1992) 136–138.

[10] R.E. Cohen, H. Krakauer, Electronic structure studies of the differences in ferroelectric behavior of $BaTiO_3$ and $PbTiO_3$, Ferroelectrics 136 (1992) 65–83.

[11] D.J. Singh, Structure and energetics of antiferroelectric $PbZrO_3$, Phys. Rev. B 52 (1995) 12559–12563.

[12] T.R. Shrout, S.J. Zhang, Lead-free piezoelectric ceramics: alternatives for PZT? J. Electroceram. 19 (2007) 113–126.

[13] M.D. Maeder, D. Damjanovic, N. Setter, Lead free piezoelectric materials, J. Electroceram. 13 (2004) 385–392.

[14] T. Takenaka, H. Nagata, Y. Hiruma, Current developments and prospective of lead-free piezoelectric ceramics, Jpn. J. Appl. Phys. 47 (2008) 3787–3801.

[15] P. Kumari, R. Rai, S. Sharma, M. Shandilya, A. Tiwari, State-of-the-art of lead free ferroelectrics: a critical review, Adv. Mater. Lett. 6 (2015) 453–484.

[16] G. Catalan, J.F. Scott, Physics and applications of bismuth ferrite, Adv. Mater. 21 (2009) 2463–2485.

[17] J. Zylberberg, A. Belik, A. Takayama-Muromachi, E. Ye, Z.-G. Bismuth Aluminate, A new high-T_C lead-free piezo-/ferroelectric, Chem. Mater. 19 (2007) 6385–6390.

[18] M.C. Stennett, I.M. Reaney, G.C. Miles, D.I. Woodward, A.R. West, C.A. Kirk, I. Levin, Dielectric and structural studies of $Ba_2MTi_2Nb_3O_{15}$ (BMTNO$_{15}$, M=Bi^{3+}, La^{3+}, Nd^{3+}, Sm^{3+}, Gd^{3+}) tetragonal tungsten bronze-structured ceramics, J. Appl. Phys. 101 (2007).

[19] H. Ma, K. Lin, L. Fan, Y. Rong, J. Chen, J. Deng, L. Liu, S. Kawaguchi, K. Kato, X. Xing, Structure and oxide ion conductivity in tetragonal tungsten bronze $BaBiNb_5O_{15}$, RSC Adv. 5 (2015) 71890–71895.

[20] A. Simon, J. Ravez, Lead-free relaxors with "TTB" structure containing either lanthanum or bismuth, Phys. Status Solidi A 199 (2003) 541–545.

[21] B. Muktha, A. Simon, J. Darriet, T.N. Guru Row, Crystal chemistry of a new solid solution in the $BaO-Bi_2O_3-Nb_2O_5$ system: $Ba_{5x/2}Bi_{(1-x)5/3}Nb_5O_{15}$, Chem. Mater. 18 (2006) 1240–1246.

[22] I.-E. Nylund, C.R. Zeiger, D. Peng, P.E. Vullum, J. Walker, M.-A. Einarsrud, T. Grande, Centrosymmetric tetragonal tungsten bronzes $A_4Bi_2Nb_{10}O_{30}$ (A = Na, K, Rb) with a Bi 6s lone pair, Chem. Mater. 35 (2022) 17–26.

[23] A. Magnéli, The crystal structure of tetragonal potassium tungsten bronze, Arkiv för Kemi 1 (1949) 213–221.

[24] K.L. Ngai, T.L. Reinecke, Model of the ferroelectric phase transition in the tetragonal tungsten-bronze-structure ferroelectrics, Phys. Rev. Lett. 38 (1977) 74–77.

[25] I.G. Ismailzade, An X-ray study of some compounds of composition $A(B'_x, B''_{2-x})O_6$, $(A'_{0.8}, A''_{0.4})Nb_2O_6$ and $(Ba_{0.4}Sr_{0.2}, Ca_{0.4})TiO_3$ (A=Sr, Ba; B'=Fe, Mg; B''=Nb; A'=K, A''= La, Bi), Sov. Phys. Crystallogr. 8 (1963) 274–277.

[26] M. Shimazu, Y. Tanokura, S. Tsutsumi, X-Ray-diffraction and dielectric studies on the $K_2BiNb_5O_{15}$-$K_2LaNb_5O_{15}$ system, Jpn. J. Appl. Phys. Part 1 28 (1989) 1877–1881.

[27] R.R. Neurgaonkar, W.K. Cory, J.R. Oliver, E.J. Sharp, G.L. Wood, G.J. Salamo, Growth and optical properties of ferroelectric tungsten bronze crystals, Ferroelectrics 142 (1993) 167–188.

[28] Y.L. Li, C. Hui, Y.X. Li, Y.L. Wang, Preparation of textured $K_2BiNb_5O_{15}$ ceramics with rod-like templates by the screen-printing technique, J. Alloy. Compd. 509 (2011) L203–L207.

[29] M.A. Bunin, O.A. Bunina, K.S. Chumachenko, Ordering of A-cations in lead-free oxides with a filled tetragonal tungsten bronze structure, J. Phys.: Conf. Ser. 1967 (2021) 8.

[30] G.H. Olsen, M.H. Sørby, S.M. Selbach, T. Grande, Role of lone pair cations in ferroelectric tungsten bronzes, Chem. Mater. 29 (2017) 6414–6424.

[31] A. Walsh, D.J. Payne, R.G. Egdell, G.W. Watson, Stereochemistry of post-transition metal oxides: revision of the classical lone pair model, Chem. Soc. Rev. 40 (2011) 4455–4463.

[32] N. Wakiya, J.K. Wang, A. Saiki, K. Shinozaki, N. Mizutani, Synthesis and dielectric properties of $Ba_{1-x}R_{2x/3}Nb_2O_6$ (R: rare earth) with tetragonal tungsten bronze structure, J. Eur. Ceram. Soc. 19 (1999) 1071–1075.

[33] X. Zhu, M. Fu, M.C. Stennett, P.M. Vilarinho, I. Levin, C.A. Randall, J. Gardner, F. D. Morrison, I.M. Reaney, A. Crystal-Chemical, Framework for relaxor versus normal ferroelectric behavior in tetragonal tungsten bronzes, Chem. Mater. 27 (2015) 3250–3261.

[34] M.G. Navarro-Rojero, J.J. Romero, F. Rubio-Marcos, J.F. Fernandez, Intermediate phases formation during the synthesis of $Bi_4Ti_3O_{12}$ by solid state reaction, Ceram. Int. 36 (2010) 1319–1325.

[35] T. Rojac, A. Bencan, B. Malic, G. Tutuncu, J.L. Jones, J.E. Daniels, D. Damjanovic, $BiFeO_3$ ceramics: processing, electrical, and electromechanical properties, J. Am. Ceram. Soc. 97 (2014) 1993–2011.
[36] I.-E. Nylund, N.S. Løndal, J. Walker, P.E. Vullum, M.-A. Einarsrud, T. Grande, Cation disorder in ferroelectric $Ba_4M_2Nb_{10}O_{30}$ (M = Na, K, and Rb) tetragonal tungsten bronzes, Inorg. Chem. 61 (2022).
[37] A.L. Hector, S.B. Wiggin, Synthesis and structural study of stoichiometric $Bi_2Ti_2O_7$ pyrochlore, J. Solid State Chem. 177 (2004) 139–145.
[38] G. Kresse, J. Furthmuller, Efficient iterative schemes for ab initio total-energy calculations using a plane-wave basis set, Phys. Rev. B 54 (1996) 11169–11186.
[39] G. Kresse, J. Furthmüller, Efficiency of ab-initio total energy calculations for metals and semiconductors using a plane-wave basis set, Comput. Mater. Sci. 6 (1996) 15–50.
[40] G. Kresse, J. Hafner, Ab initio molecular dynamics for liquid metals, Phys. Rev. B 47 (1993) 558–561.
[41] G. Kresse, J. Hafner, Ab initio molecular-dynamics simulation of the liquid-metal-amorphous-semiconductor transition in germanium, Phys. Rev. B 49 (1994) 14251–14269.
[42] P.E. Blöchl, Projector augmented-wave method, Phys. Rev. B 50 (1994) 17953–17979.
[43] J.P. Perdew, K. Burke, M. Ernzerhof, Generalized gradient approximation made simple, Phys. Rev. Lett. 77 (1996) 3865–3868.
[44] J.P. Perdew, A. Ruzsinszky, G.I. Csonka, O.A. Vydrov, G.E. Scuseria, L. A. Constantin, X. Zhou, K. Burke, Restoring the density-gradient expansion for exchange in solids and surfaces, Phys. Rev. Lett. 100 (2008) 136406.
[45] S.S. Aamlid, S.M. Selbach, T. Grande, The effect of cation disorder on ferroelectric properties of $Sr_xBa_{1-x}Nb_2O_6$ tungsten bronzes, Materials 12 (2019).
[46] S.S. Aamlid, S.M. Selbach, T. Grande, Structural evolution of ferroelectric and ferroelastic barium sodium niobate tungsten bronze, Inorg. Chem. 59 (2020) 8514–8521.
[47] G.H. Olsen, U. Aschauer, N.A. Spaldin, S.M. Selbach, T. Grande, Origin of ferroelectric polarization in tetragonal tungsten-bronze-type oxides, Phys. Rev. B 93 (2016).
[48] N.S. Løndal, B.A.D. Williamson, J. Walker, M.-E. Einarsrud, T. Grande, The effect of cation size on structure and properties of Ba-based tetragonal tungsten bronzes $Ba_4M_2Nb_{10}O_{30}$ (M=Na, K or Rb) and $Ba_4M_2Nb_8Ti_2O_{30}$ (M=Ca or Sr), Phys. Chem. Chem. Phys. (2024). Advance Article.
[49] G.J. Limburn, D.W. Davies, N. Langridge, Z. Malik, B.A.D. Williamson, D. O. Scanlon, G. Hyett, Investigation of factors affecting the stability of compounds formed by isovalent substitution in layered oxychalcogenides, leading to identification of $Ba_3Sc_2O_5Cu_2Se_2$, $Ba_3Y_2O_5Cu_2S_2$, $Ba_3Sc_2O_5Ag_2Se_2$ and $Ba_3In_2O_5Ag_2Se_2$, J. Mater. Chem. C 10 (2022) 3784–3795.
[50] B.A.D. Williamson, G.J. Limburn, G.W. Watson, G. Hyett, D.O. Scanlon, Computationally driven discovery of layered quinary oxychalcogenides: potential p-type transparent conductors? Matter 3 (2020) 759–781.
[51] A. Jain, S.P. Ong, G. Hautier, W. Chen, W.D. Richards, S. Dacek, S. Cholia, D. Gunter, D. Skinner, G. Ceder, et al., Commentary: the materials project: a materials genome approach to accelerating materials innovation, APL Mater. 1 (2013).
[52] W. Sun, S.T. Dacek, S.P. Ong, G. Hautier, A. Jain, W.D. Richards, A.C. Gamst, K. A. Persson, G. Ceder, The thermodynamic scale of inorganic crystalline metastability, Sci. Adv. 2 (2016) e1600225.
[53] B.A.D. Williamson, J. Buckeridge, J. Brown, S. Ansbro, R.G. Palgrave, D. O. Scanlon, Engineering valence band dispersion for high mobility p-type semiconductors, Chem. Mater. 29 (2016) 2402–2413.
[54] B.A.D. Williamson, J. Buckeridge, N.P. Chadwick, S. Sathasivam, C.J. Carmalt, I. P. Parkin, D.O. Scanlon, Dispelling the myth of passivated codoping in TiO_2, Chem. Mater. 31 (2019) 2577–2589.
[55] F. Li, S.J. Zhang, D. Damjanovic, L.Q. Chen, T.R. Shrout, Local structural heterogeneity and electromechanical responses of ferroelectrics: learning from relaxor ferroelectrics, Adv. Funct. Mater. 28 (2018) 1801504.
[56] C.C. Homes, T. Vogt, S.M. Shapiro, S. Wakimoto, A.P. Ramirez, Optical response of high-dielectric-constant perovskite-related oxide, Science 293 (2001) 673–676.
[57] P. Lunkenheimer, R. Fichtl, S.G. Ebbinghaus, A. Loidl, Nonintrinsic origin of the colossal dielectric constants in $CaCu_3Ti_4O_{12}$, Phys. Rev. B 70 (2004).
[58] S. Stølen, T. Grande, Chemical Thermodynamics of Materials: Macroscopic and Microscopic Aspects, John Wiley & Sons, Ltd., Chichester, West Sussex, England, 2003.
[59] D.M. Giaquinta, H.-C. zur Loye, Structural predictions in the ABO_3 phase diagram, Chem. Mater. 6 (1994) 365–372.
[60] K. Lin, Z. Zhou, L. Liu, H. Ma, J. Chen, J. Deng, J. Sun, L. You, H. Kasai, K. Kato, et al., Unusual strong incommensurate modulation in a tungsten-bronze-type relaxor $PbBiNb_5O_{15}$, J. Am. Chem. Soc. 137 (2015) 13468–13471.
[61] R.D. Shannon, Revised effective ionic-radii and systematic studies of interatomic distances in halides and chalcogenides, Acta Crystallogr. Sec. A 32 (1976) 751–767.
[62] A.M. Hardy, A. Hardy, G. Ferey, Structure cristalline du bronze pseudo-quadratique $K_{0.6}FeF_3$: transition pyrochlore-quadratique pour les composés $KMM'X_6$, Acta Crystallogr. B 29 (1973) 1654–1658.
[63] J. Gardner, F.D. Morrison, A-site size effect in a family of unfilled ferroelectric tetragonal tungsten bronzes: $Ba_4R_{0.67}Nb_{10}O_{30}$ (R = La, Nd, Sm, Gd, Dy and Y), Dalton Trans. 43 (2014) 11687–11695.
[64] V.M. Goldschmidt, Die Gesetze der Krystallochemie, Die Nat. 14 (1926) 477–485.
[65] C. Li, X. Lu, W. Ding, L. Feng, Y. Gao, Z. Guo, Formability of ABX_3 (X = F, Cl, Br, I) halide perovskites, Acta Crystallogr. B 64 (2008) 702–707.
[66] G. Kieslich, S. Sun, A.K. Cheetham, Solid-state principles applied to organic–inorganic perovskites: new tricks for an old dog, Chem. Sci. 5 (2014) 4712–4715.
[67] H.D. Megaw, Crystal structure of double oxides of the perovskite type, Proc. Phys. Soc. Lond., Sect. B 58 (1946) 133–152.
[68] A. Bencan, E. Oveisi, S. Hashemizadeh, V.K. Veerapandiyan, T. Hoshina, T. Rojac, M. Deluca, G. Drazic, D. Damjanovic, Atomic scale symmetry and polar nanoclusters in the paraelectric phase of ferroelectric materials, Nat. Commun. 12 (2021) 3509.
[69] R.D. Shannon, Dielectric polarizabilities of ions in oxides and fluorides, J. Appl. Phys. 73 (1993) 348–366.
[70] X. Wu, L. Wen, C. Wu, X. Lv, J. Yin, J. Wu, Insight into the large electro-strain in bismuth sodium titanate-based relaxor ferroelectrics: from fundamentals to regulation methods, J. Mater. Sci. Technol. 150 (2023) 27–48.
[71] N. Raengthon, T. Sebastian, D. Cumming, I.M. Reaney, D.P. Cann, J. Roedel, $BaTiO_3$-$Bi(Zn_{1/2}Ti_{1/2})O_3$-$BiScO_3$ceramics for high-temperature capacitor applications, J. Am. Ceram. Soc. 95 (2012) 3554–3561.
[72] D.H. Choi, A. Baker, M. Lanagan, S. Trolier-McKinstry, C. Randall, D. Johnson, Structural and dielectric properties in $(1-x)BaTiO_3$-$xBi(Mg_{1/2}Ti_{1/2})O_3$ ceramics ($0.1 \leq x \leq 0.5$) and potential for high-voltage multilayer capacitors, J. Am. Ceram. Soc. 96 (2013) 2197–2202.
[73] J. Rödel, K.G. Webber, R. Dittmer, W. Jo, M. Kimura, D. Damjanovic, Transferring lead-free piezoelectric ceramics into application, J. Eur. Ceram. Soc. 35 (2015) 1659–1681.
[74] Z. Lazarevic, B.D. Stojanovic, J.A. Varela, An approach to analyzing synthesis, structure and properties of bismuth titanate ceramics, Sci. Sinter. 37 (2005) 199–216.
[75] M. Gröting, K. Albe, Theoretical prediction of morphotropic compositions in $Na_{1/2}Bi_{1/2}TiO_3$-based solid solutions from transition pressures, Phys. Rev. B (2014) *89*.